We are IntechOpen, the world's leading publisher of Open Access books
Built by scientists, for scientists

6,900
Open access books available

186,000
International authors and editors

200M
Downloads

Our authors are among the

154
Countries delivered to

TOP 1%
most cited scientists

12.2%
Contributors from top 500 universities

CLARIVATE ANALYTICS
BOOK CITATION INDEX
INDEXED

WEB OF SCIENCE™

Selection of our books indexed in the Book Citation Index in Web of Science™ Core Collection (BKCI)

Interested in publishing with us?
Contact book.department@intechopen.com

Numbers displayed above are based on latest data collected.
For more information visit www.intechopen.com

Chapter 14

Study of Carbon Nanotube Based Devices Using Scanning Probe Microscope

Hock Guan Ong and Junling Wang

Additional information is available at the end of the chapter

http://dx.doi.org/10.5772/52067

1. Introduction

Since the discovery in 1991 [1], carbon nanotube (CNT) has gained widespread attention. Many researchers have been uncovering the charaterizatics of this 1D material which possesses excellent electrical, mechanical and chemical properties. Single walled CNT has a diameter ranging from 3 Å to a few nanometer, which makes the fabrication and charaterization of CNT based devices much more difficult. There is a need for techniques that are suitable for nanometer scale charaterizations for better understanding of CNT based devices. Atomic force microscope (AFM) is powerful equipment for this purpose. In its basic mode of operation, it can reveal the morphology of CNT based devices with nanometer resolution. Moreover, various enhanced modes of operation make it possible to investigate the different properties of CNT as well as the performance of CNT based devices. In this chapter, we focus on two similiar techniques: electrostatic force microscpy (EFM) and Kelvin probe force microscpy (KPFM, alson know as scanning Kelvin probe microscopy (SKPM)). We will introduce the operation principles of these two techniques and review our recent studies on CNT using EFM. Studies conducted by other groups are also reviewed.

1.1. History of atomic force microscope

In 1972, Russell Young demonstrated surface imaging by measuring the electrical current between the sample and a scanning probe.[2] Even though the technique did not take off immediately, interest in achieving atomic resolution in surface characterization persisted in the scientific community. In 1981, Gerd Binning and Heinrich Rohr from IBM succeeded and gave birth to the first scanning tunneling microscope (STM).[3] In this system, the tunneling current between the sample and a scanning tip hovering a few angstroms above the surface is used to obtain the topography information. They later obtained image of the 7 × 7 reconstruc-

INTECH
open science | open minds

© 2013 Ong and Wang; licensee InTech. This is an open access article distributed under the terms of the Creative Commons Attribution License (http://creativecommons.org/licenses/by/3.0), which permits unrestricted use, distribution, and reproduction in any medium, provided the original work is properly cited.

tion of silicon surface with atomic resolution in 1983.[4] In 1986, they were jointly awarded the Nobel Prize in Physics "for their design of the scanning tunneling microscope".[5]

Despite the atomic scale resolution of STM, the strict operation enviroment requirements such as high vacuum and clean surface limit its application. There is need for an easy-to-use surface characterization system. In 1986, Binning, Quate and Gerber invented the first AFM which can operate under ambient conditions.[6] The full history of STM and AFM can be found in many textbooks and reviews.[see for example, ref 7]

Atomic force microscope possesses several unique advantages over other techniques such as STM and scanning electron microscopy (SEM), including its capability to operate in different environments (vacuum, ambient and liquid), simple sample preparation and its capability to incorporate local electrical or magnetic measurements. Figure 1 (a) describes schematicaly the imaging mechanism of an AFM. For topography measurement, it can operate under contact or tapping mode. In contact mode, the tip is in direct contact with the sample surface during the scan. The position of the reflected laser spot on the photodiode changes as the tip being deflected by the surface morphology. Using this photodiode signal, the z axis piezoelectric stack will tune the height of the tip (in some AFMs, the height of the sample is changed instead) to maintain a constant deflection. The z-piezoelectric movements at different locations give rise to the topography image. In tapping mode, the tip is mechanically driven by a piezoelectric actuator to oscillate around its resonance frequency and is only tapping on the sample surface during the scan. Figure 1 (b) depicts the tapping mode operation. The oscillation of the cantilever leads to the same oscillation of the laser spot on the photodiode, which is used as the feedback signal for the z axis piezoelectric stack. When the tip scans along the surface of a sample, the z axis piezoelectric stack will move the cantilever (or the sample) up and down to maintain a constant oscillation amplitude. The movement of the z axis piezoelectric stack is used to construct the surface profile of the sample. For further discussion about the operation of an AFM, the readers are referred to ref 8.

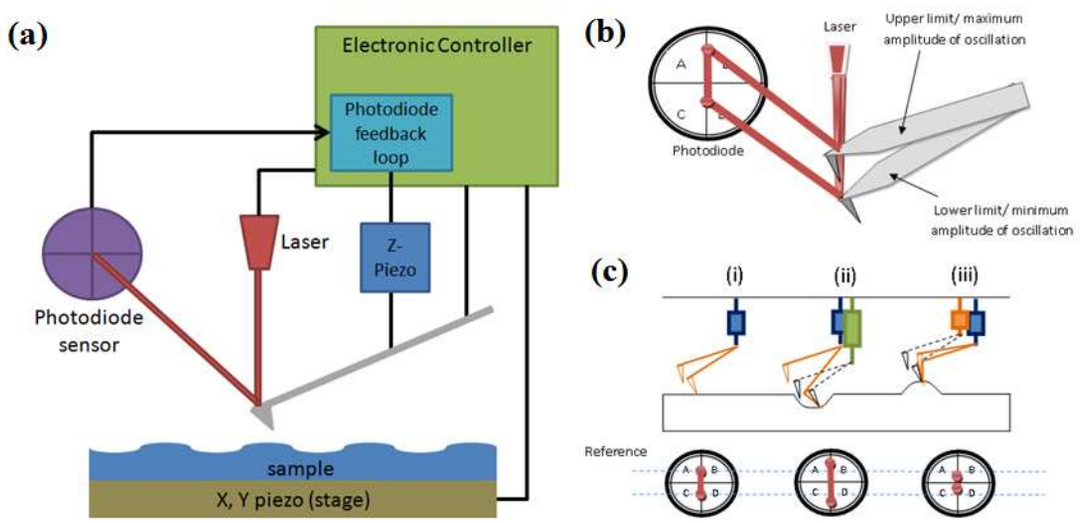

Figure 1. (a) Schematic description of an AFM. (b) Cantilever deflection and laser spot on the photodiode, (c) schematic of the tapping mode operation.

In the normal topography measurement, the AFM tip only senses the intermolecular force between the sample surface and the tip. By adjusting the scanning method, other interactions such as electrostatic and magnetostatic forces between the tip and sample can also be measured. Some of these techniques include EFM, KPFM, piezoelectric force microscopy (PFM), magnetic force microscopy (MFM), etc. In this chapter, we will forcus on EFM and KPFM and their application in the characterization of CNT based devices.

1.2. Principles of EFM and KPFM

Atomic force microscope based techniques offer unique advantages for the study of nanoelectronic devices because of their high resolution. In particular, EFM and KPFM are sensitive to local potential and space charges. Their operation principles are very similiar. They are both dual path tapping mode techniques, as shown in Figure 2 (a), and use a conductive tip for the scans. During the first scan, the system operates as per the normal tapping mode, recording the topography of the sample. During the second scan, the tip is lifted by a fixed height (usually a few tens of nanometers) from the sample surface. It then retraces the surface profile recorded in the first scan, while maintaining the lift height.

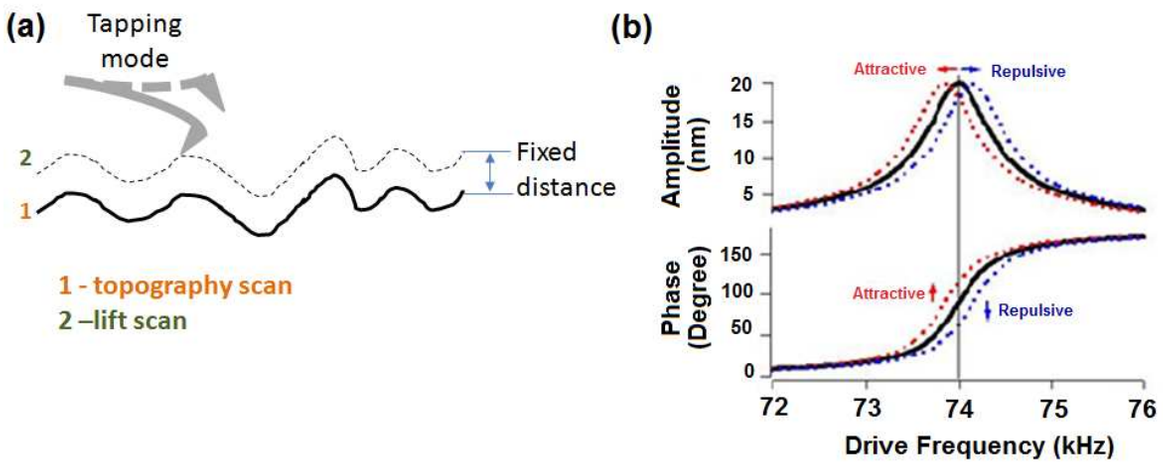

Figure 2. (a) Schematic description of the dual-pass technique. (b) Effects of attractive and repulsive forces on the cantilever oscillation amplitude and phase. [9].

For EFM, a DC bias is applied to the tip during the second scan, so that the long range electrostatic force, if any, between the sample and the tip can be detected. The electrostatic force acting on the tip will cause the resonance frequency of the cantilever to shift as indicated in Figure 2 (b). Since the cantilever is driven at its original free-standing resonance frequency, the vibration amplitude and phase will change. For example, if a positive bias is applied to the tip, it will experience a net repulsive force if positive charges exist on the surface of the sample. This will reduce the cantilever oscillation amplitude and decrease its phase shift with respect to the driving signal as shown in Figure 2 (b). On the other hand, negative charges will increase the phase shift. Thus we could tell the type of charges by looking at the

phase shift of the cantilever oscillation. Mathematically, the phase changes due to the force acting on the cantilever is given by the following equation: [8]

$$\Delta\varphi = -\arcsin\left(\frac{Q}{k}\frac{dF}{dz}\right) \tag{1}$$

where k is the spring constant and Q is the quality factor of the cantilever.

Under normal condition, capacitive coupling force between the tip and sample dominates during the second scan, which is represented by

$$F(z) = \frac{1}{2}\frac{dC}{dz}V_{dc}{}^{2} \tag{2}$$

When net charges exist on the sample surface, electrostatic force between them and their image charges in the tip also contributes [10], so

$$F(z) = \frac{1}{2}\frac{dC}{dz}V_{dc}{}^{2} + \frac{q_s q_s^{'}}{4\pi\varepsilon_0 (z+z^{'})^2} + \frac{q_s C V_{dc}}{4\pi\varepsilon_0 (z+r)^2} \tag{3}$$

where r is the radius of the tip. The first term on the right hand side of the equation represents the capacitive coupling force. The second term comes from the surface charges and their image charges located at z' in the tip. The third term comes from the interaction between the surface charges and tip bias.

It has been reported that EFM can reach a resolution of ~20 nm,[11] thus is a very useful tool to study nanoelectronic devices.[12,13] Various groups have used this technique to study charge distribution,[14,15,16] defects, [17] and electrical transport. [18]

As for KPFM, it reveals the built-in potential difference between two materials when they are electrically connected. This is usually generated due to the different work functions, φ, of them. When connected, electrons will redistribute to equalize the Fermi levels and generate a built-in field across the interface. In KPFM, an external dc voltage,V_{dc}, is applied between the the tip and the sample to neutralize the built-in field. If there is no static charges involved and the reference material's work function is known, the other material's work function can be calculated as $\varphi_2 = \varphi_1 - qV_{ext}$, as shown in Figure 3.

In amplitude modulated KPFM, the setup and scan process are the same as EFM. However, during the second scan, the cantilever is not oscillated mechanically. Instead, an AC bias of frequency ω, V_{ac}, is applied to the tip, which drives the tip to oscillate at the same frequency due to capacitive coupling. This oscillation can be detected by the photodiode and is feedback to the controller. A DC bias, V_{dc}, is applied to cancel the built-in potential and the oscillation.

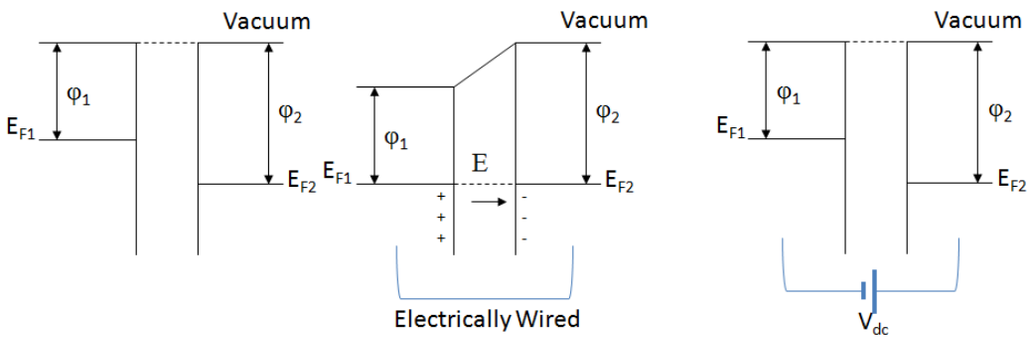

Figure 3. Build-in potential difference due to work function difference.

Approximate the tip-sample system as a parrallel plate capacitor, we can write its energy U as

$$U = \frac{1}{2} C \Delta V^2 \tag{4}$$

where C is the capacitance. The voltage between the tip and sample has three conmponents, the potential arises due to work function difference and static charges if any, the V_{dc} supplied and the oscillating V_{ac}, it can be written as:

$$\Delta V = \Delta\varphi - V_{dc} + V_{ac} \sin(\omega t) \tag{5}$$

At small oscillation amplitude, the force between the tip and sample is

$$F(z) = -\frac{\partial U}{\partial z} = -\frac{1}{2}\frac{\partial C}{\partial z}\Delta V^2 = F_{dc} + F_{\omega} + F_{2\omega} \tag{6}$$

where

$$F_{dc} = -\frac{1}{2}\frac{\partial C}{\partial z}\left[(\Delta\varphi - V_{dc})^2 + \frac{V_{ac}^2}{2}\right] \tag{7}$$

$$F_{\omega} = -\frac{\partial C}{\partial z}(\Delta\varphi - V_{dc})V_{ac} \sin(\omega t) \tag{8}$$

$$F_{2\omega} = -\frac{1}{4}\frac{\partial C}{\partial z}V_{ac}^2 \cos(2\omega t) \tag{9}$$

When V_{dc} equals to the potential difference between the sample and tip, the oscillation at frequency ω is zero. So the V_{dc} values applied to cancel the oscillation at different locations of the sample represent the local surface potential variation across the sample.

2. Application of AFM based techniques in the study of CNT and CNT based devices

Techniques of studying electrostatic force with force microscopes have been proposed and investigated back in 1988.[19,20,21] Detection of electrostatic force of as low as 10^{-10} N has been acheived.[19] Weaver and Abraham demonstrated that using attractive-mode force potentiometry, detection of sub-millivolt signal can be acheived with spatial resolution of ~ 50 nm.[20] These early works laid the foundation of EFM. It had since improved further and reached resolution of 20 nm under ambient condition.[22] In 1991, KPFM based on volatage modulation was introduced.[23]

2.1. Seeing the CNTs more clearly

The basic capability of EFM can be demostrated in Figure 4, where both the topography and EFM signal of a SiO_2/Si substrate with CNTs on the surface are shown. Clearly, the surface roughness makes it difficult to identify the CNTs in the topography image, but they are clearly seen in the EFM image in Figure 4 (b). Furthermore, we can also identify CNTs that are connected to electrode (not shown in the figure) biased at 3 V (which are brighter) and those that are not connected. In this experiment, we have intentionally cut the CNTs by scratching the surface using a diamond cutter. Clear sharp contrast is observed at the scratch mark where the CNTs are broken. This demonstrated that EFM is an excellent tool to study CNT based nanodevices.

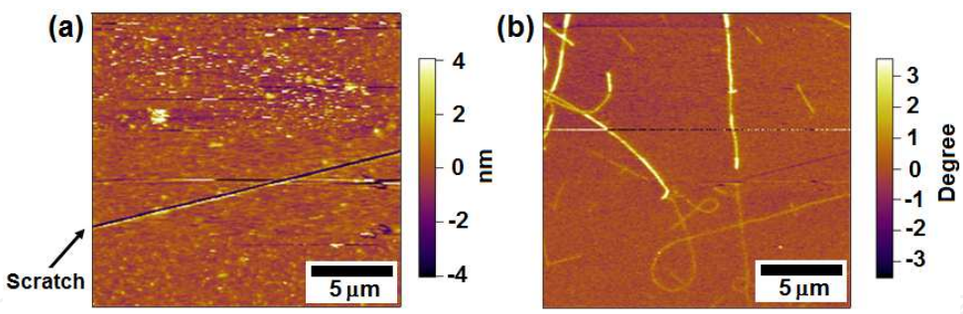

Figure 4. (a) Topography of Si substrate with CNTs on the surface. (b) EFM phase image of the same area clearly show the CNTs. The discontinuity of the CNT at the scratch mark can be observed. The electrode (not seen in the figure) is biased at 3V.

Compared with other surface characterization tools such as AFM and SEM, another advantage of EFM is that it can image CNTs that are embedded in a dielectric material noninvasively because it senses long range electrostatic force. This is especially useful for the study of CNT composite materials. For example, Jespersen *et al.* reported the mapping of individual CNT in poly-methylmethacrylate (PMMA) matrix. They have studied the EFM response vs tip-CNT distance relationship using a ~ 170 nm thick trilayer sample comprising of composite-PMMA-composite (60 nm/50 nm/60 nm) as shown in Figure 5. They used a tip bias of 7 V and lift height of 35 nm. Figure 5 (a) shows two CNTs, T_1 and T_2, locating at the top and

bottom layer, respectively. Obtaining the dependence of EFM signal on tip-CNT distance allows them to estimate the the depth position of CNTs. It was reported that this subsurface characteriztion can reach a depth of 300 nm, and it is capable of 3 dimensional mapping of CNTs in the polymer matrix as shown in Figure 5 (c).[24] Subsequently, Zhao *et al.* investigated the parameters that may affect the study of polymer-CNT composite via EFM.[25] He noted that reducing humdity increases the EFM signal and improves the subsurface imaging capability. This was attributed to a reduction in the thin water layer adsorbed on the tip and sample surface, which reduces the electric field penetrating into the polymer. They also suggested that EFM subsurface imaging is useful to study high dielectric constant nanostructures in a matrix that has low dielectric constant.

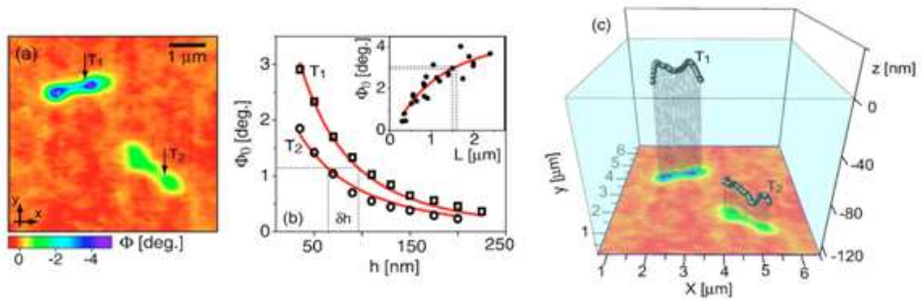

Figure 5. (a) EFM image showing two SWCNTs embedded in a ~170 nm thick film of SWCNT/PMMA composite. (b) The lift-height dependence of the length-corrected EFM signal of the two tubes in (a). The measurements were performed at the points indicated in (a). The measured amplitudes have been fitted to $\Phi(x) = A/(h+h_0)^3$. The inset shows Φ_0 vs nanotube length L for 30 isolated SWCNTs measured with known tip-tube separation h=60 nm. The red line shows a fit to the theoretical prediction $\Phi_0 \ ^{-1/2}\alpha \ l^{-1}$. (c) A projection view of the three dimensional map of the two nanotubes as inferred from the data in (a) and (b). The blue region illustrates the PMMA matrix. Reprinted with permission from [24]. Copyright 2012, American Institute of Physics.

2.2. Distinguish different types of CNTs

A CNT can be either metallic or semiconducting depending on its chirality. Both types usually coexist in the as grown CNTs, which is problematic for subsequent fundamental study, device fabrication and applications. Therefore, it is very important to diferentiate the different types of CNTs without means of electrical measurements.

Lu *et al.* have used KPFM (the authors called it EFM in their paper) to seperate different types of CNTs through measuring their dielectric responses.[26] This can be acheived because metallic CNTs have a larger dielectric response than semiconducting ones. To measure the difference, a volage of $V = V_{dc} + V_{ac} \sin(\omega t)$, where $V_{ac} = 5\ V_{rms}$, is applied to the tip duing the lift scan. V_{dc} is used to nullify the contact potential difference between the tip and sample. The AC bias, V_{ac}, will create a dynamic polarization in the CNT, which interacts with the tip and gives rise to an attractive force that oscillates at the frequency of 2ω. This 2ω deflection signal is proportional to the dielectric constant of CNT, and it can be plotted against the square of the tube diameter, D_2 as shown in Figure 6. The difference between metalic and semiconducting CNTs are clearly seen in Figure 6(c).

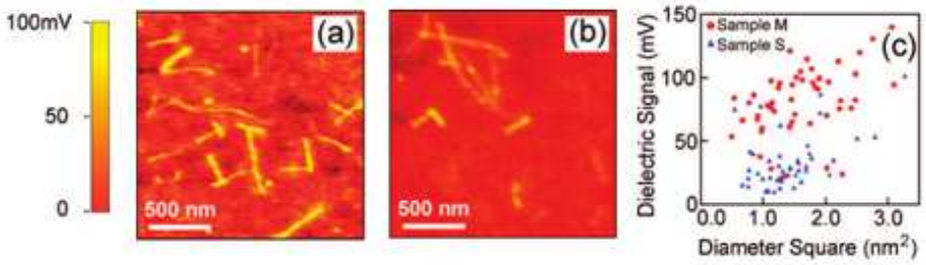

Figure 6. (a) and (b) Representative dielectric response images of semiconducting and metallic-tube-enriched samples S and M, respectively. (c) Dielectric response vs D^2 plot. Reprinted with permission from [26] Copyright 2012 American Chemical Society.

More interestingly, EFM can be used to study the dynamic tuning of CNT bandgap. It has been predicted theoretically that mechanical deformation of CNT will lead to the opening and/or closure of the bandgap.[27] And Barboza *et al.* has used EFM to study this deformation induced metal-semiconductor transition in CNT.[28]

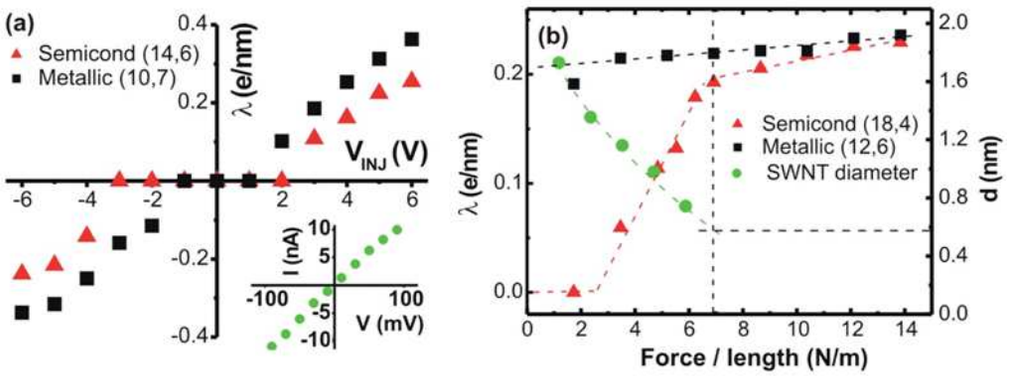

Figure 7. (a) Plot of the charge density (in electrons/nm) as a function of injection bias V_{INJ} for a (10,7) metallic nanotube (black squares) and a (14, 6) semiconducting nanotube (red triangles). The inset shows an I(V) curve acquired with the tip in contact with a thin metallic (Mo) film. (b) Plot of the charge density as function of the applied compressive force per unit length for (12,6) metallic nanotube (black squares) and (18,4) semiconducting nanotube (red triangles). The evolution of the apparent height (diameter) of the (18,4) semiconducting SWNT with applied force is also plotted in this graph (green circles). The dashed lines are guides for the eye. Reprinted figure with permission from [28]. Copyright 2012 by the American Physical Society. [1]

They first identified the nature of the CNTs using Raman spectroscopy and a pair of metallic and semiconducting CNTs with similiar diameters were chosen for the subsequent study. A compressive force is applied to the CNTs (on SiO_2) using the tip, and a bias is applied simutaneously to inject charges into the CNTs. EFM is then conducted with a tip bias of 0 V during the lift scan, this allows the authors to obtain the injected charges quantatively. From the

1 Readers may view, browse, and/or download material for temporary copying purposes only, provided these uses are for noncommercial personal purposes. Except as provided by law, this material may not be further reproduced, distributed, transmitted, modified, adapted, performed, displayed, published, or sold in whole or part, without prior written permission from the American Physical Society.

http://dx.doi.org/10.5772/52067

injected charge density vs bias, V_{INJ}, plot in Figure 7 (a), it is noted that metallic and semiconducting CNTs shows similiar features. But the plot is symmetric for metallic CNT with a threshold bias of ~ ±2V, while it is asymmetric for the semiconcducting CNT. Thus, there exists a bias voltage (-3 V) where metallic CNTs will show charging but semiconducting CNTs won't. Subsequently, they measured the charge density in a CNT as a function of the compressive force applied. As seen in Figure 7 (b), charge density in metallic CNT has a very weak dependance on the applied compressive force, while the semiconducting CNT shows significant changes between 2 to 7 N/m. With increasing compressive force on the semiconducting CNT, the charge density increases from zero and saturates at a similiar level as in the metallic CNT. It was concluded that compression can induce semiconducting to metallic transition in a CNT. The diameter of the CNT also decreases under compressive force until the threshold value when semiconducting-metallic transition occurs.

2.3. In-situ study of CNT based devices using EFM

2.3.1. Interface in CNT based devices.

Because of its capability to map charge and potential variations at nanometer scale, EFM is an ideal tool to study the electrical characteristics of CNT based devices. For example, Bachtold *et al.* have reported their study on the contact resistance between CNT and metal electrodes.[18] They used EFM to obtain the potential drop across the channel of a carbon nanotube field effect transistor (CNT FET) while a bias is applied to one of the electrodes as shown in Figure 8. By comparing the EFM signal drop against a known voltage, the contact resistance and the intrinsic resistance of the CNT can be obtained. It was observed that the potential drop across a multi walled CNT is uniform, indicating that it behaves as a diffusive condutor. Using this technique, they also determined that the intrinsic resistance of a two metallic CNTs bundle is 3 kΩ at the most. Combining the measured value with the four-terminal Landauer formula, they concluded that the "transport in metallic nanotubes is ballistic over a lenght of > 1 μm, even at room temperature." [18]

Besides using EFM to measure the electical resistance in CNT based devices, researchers have also used KPFM to study the band offset at metal/CNT contacts. Shiraishi *et al.* have reported that the shift of vacuum level of single walled CNT is +5.2 meV in their CNT/Au system.[29] When tetracyano-pquinodimethane (TCNQ) molecules are used as p-type dopants, the energy band of the single walled CNT will be shifted. Using KPFM, they are able to capture the corresponding shift of vacuum level from +5.2 meV to -52 meV.

Another interesting example of EFM application in the study of CNT is the charge trapping experiments conducted by Jespersen and Nygård.[30] They observed that surface static charges can be effectively trapped within CNT loops and they can be removed by touching with a ground conductive AFM tip. These static charges were suggested to cause hysteretic behaviour in CNT FETs.

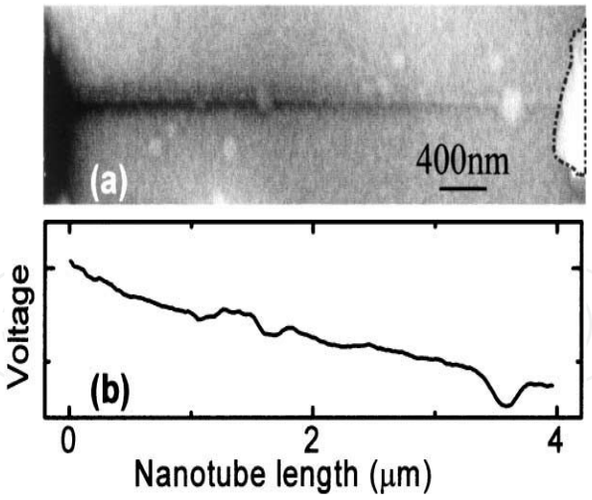

Figure 8. (a) ac-EFM image of a MWNT of diameter 9 nm. The resistance of the entire circuit is 42 kV. An ac bias of 150 mV is applied to the left electrode; the IV characteristic verified that this bias was within linear response. (b) ac-EFM signal as a function of the nanotube length. Reprinted figure with permission from [18]. Copyright 2012,the American Physical Society.[2]

2.3.2. Origin of hysteresis in CNT FET: an in-situ EFM study

Single walled CNT FET and prototype logic devices have been studied extensively.[31] However, hysteresis in the transfer characteristic exists in many of the CNT FETs reported so far.[32,33] It is detrimental for digital logic applications, but may be utilized in non-volatile memory devices.[34,35,36] Thus, it is important to understand the origin of the hysteresis, and to eliminate or stabilize it for different purposes.

To clarify the origin of hysteresis in CNT FET, we have conducted in-situ EFM study using the setup schematically shown in Figure 9 (a). For sample preparation and experimental details, please refer to [40]. This setup allows us to observe the charge activities around the CNT channel while the transfer charateristic of the device is being measured. We swept the gate bias, V_{gs}, from 25 V to -25 V and back. A hysteresis loop was observed as shown in Figure 9 (b). During the electrical measurements, EFM scans were performed at every 5 V intervals, with the V_{ds} and V_{gs} turned off temporarily during the scan. The EFM scans were conducted with tip bias of 3 V during its lifted scan and each image took ~ 40 s to complete. These images were displayed on the sides of the transfer loop in Figure 9 (b). In our system, the bright and dark contrasts represent negative and positive charges on the SiO_2 surface, respectively. After a gate bias of 25 V is applied, bright regions appear next to the CNT channel, indicating negative charge accumulation. It is emphasized that since the source, drain and gate were all connected to ground during the EFM scan, the contrast observed by the side of the CNT are due to residual charges on the surface of the SiO_2. Even as the gate bias was de-

2 Readers may view, browse, and/or download material for temporary copying purposes only, provided these uses are for noncommercial personal purposes. Except as provided by law, this material may not be further reproduced, distributed, transmitted, modified, adapted, performed, displayed, published, or sold in whole or part, without prior written permission from the American Physical Society.

http://dx.doi.org/10.5772/52067

creased to zero, the bright regions remain. As the V_{gs} polarity is reversed, dark region then first starts to appear around the CNT before extending gradually into the bright region. This suggests that the surface charges are likely injected from the CNT channel onto the SiO_2 surface. As the negative gate bias continues to increase, the bright regions disappear gradually until at V_{gs} = -25 V, where they disappears completely. The dark region, indicating positive charge accumulation, remains even when the gate bias is increased back to zero.

These injected surface charges cannot be dissipated immediately as the gate bias changes. Thus they will screen the CNT from the gate bias, causing a shift in the threshold voltage. In order to have a better understanding of the relationship between the injected charges and the hysteresis in the transfer characteristic, we performed a semi-quantitative analysis by examining the EFM phase shift distribution around CNT as shown in Figure 10 (a) and (b). Since EFM phase shift is directly related to surface charge density,[37] we can obtain qualitatively the total injected charge effect by integrating the EFM phase shift over r, the distance away from the CNT.[38] A clear hysteresis is observed (Figure 10 (c)) when the integrated value of Figure 10 (a) and (b) are plotted against gate bias, consistent with the transfer characteristic. This is expected since the screening effect should be proportional to the total amount of injected charges. Interestingly, it is observed that the amount of positive charges injected onto the surface under negative gate bias is significantly less than the negative charges under positive gate bias. This is consistent with the shift of the hysteresis loop towards positive bias side (Figure 9 (b)) and indicates that the SiO_2 surface can trap electrons more effectively than holes, consistent with other report.[39]

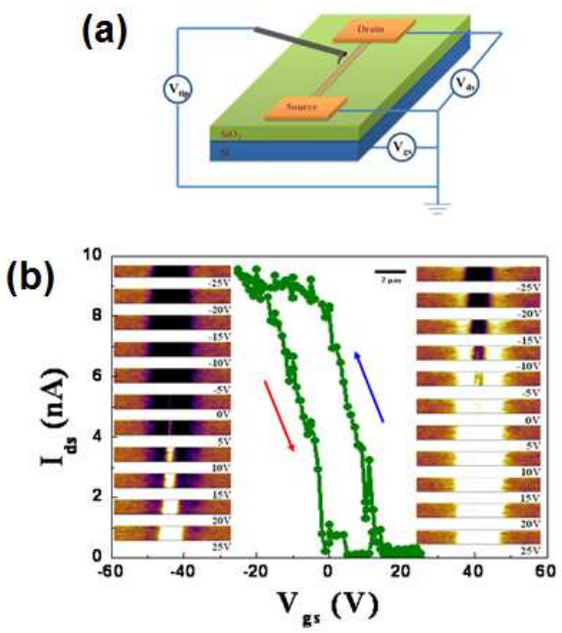

Figure 9. (a) Experiment setup for the in-situ EFM study. (b) Transfer characteristic and charge injection of a CNT FET. Transfer curve obtained by sweeping the gate bias from 25 V to – 25 V and back. The EFM images are taken at 5 V intervals. The gate bias is temporally turned off during EFM scan. Injected charges are observed around the CNT and are correlated to the hysteresis loop. Reprinted with permission from [40] Copyright 2012 IOP Publishing.

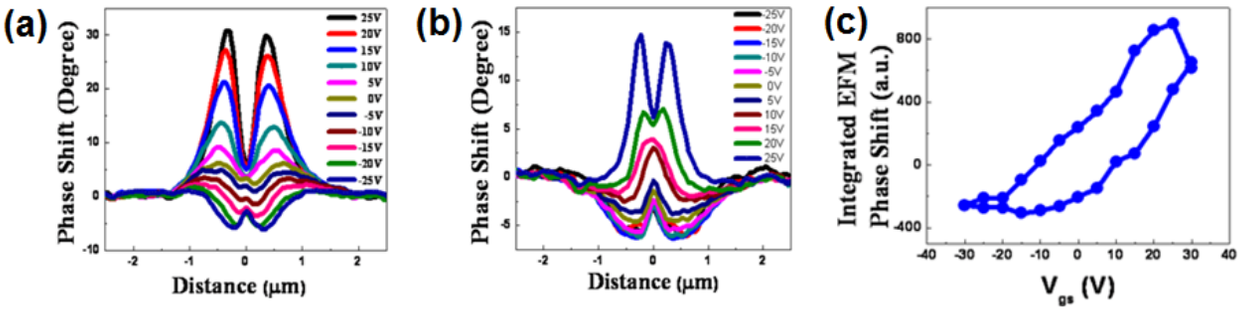

Figure 10. The cross section profiles of the EFM images, indicating the relative charge density around the CNT for (a) backward gate sweeping from 25 V to -25 V, (b) forward gate sweeping from -25 V to 25 V. (c) Integration of the phase shift, over the scan range, where r is the distance away from the CNT channel. Reprinted with permission from [40] Copyright 2012, IOP Publishing.

If the injected charges are indeed responsible for the formation of the hysteresis loop, a hysteresis-free transfer curve will be obtained if a long enough dissipation time is given before the measurement of the I_{ds}. To confirm this prediction, we repeated the same experiment with different dissipation time (Figure 11). During the measurement, the gate bias was turned off for a duration of 0 (black curve), 2 (red curve) and 15 (blue curve) minutes at every voltage step, after which it was turned back on and I_{ds} was measured immediately. It is apparent from Figure 11 (a) that longer discharging time leads to a decrease in the hysteresis width. With a discharging duration of 15 minutes, an almost hysteresis-free transfer curve was obtained. Figure 11(b) depicts the corresponding EFM images at the different discharging duration. It is obvious that the injected charges have almost disappeared completely after 15 minutes, consistent with the macroscopic transfer behavior. The remaining narrow hysteresis observed in the transfer curve is due to the little amount of residual charges (Figure 11 (c), decreased scale).

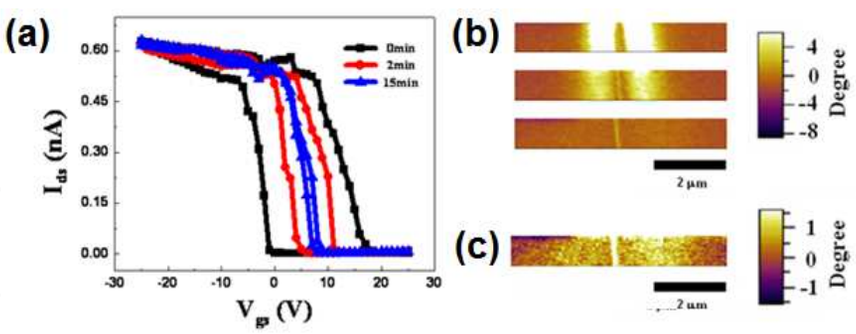

Figure 11. Hysteresis-free transfer curve under ambient condition. (a) Hysteresis width can be reduced by allowing the injected charges to dissipate at every gate bias. The experiment was conducted by turning the gate bias off at every step for 0 (black), 2 (red) and 15 (blue) minutes, and measure the Ids immediately after turning the gate bias back on. (b) The corresponding EFM images after 0 (top), 2 (middle) and 15 (bottom) minutes discharging time. (c) The bottom image in (b) replotted with reduced scale. A small amount of injected charges is observed. Reprinted with permission from [40] Copyright 2012, IOP Publishing.

Based on the above observations, a dynamic screening effect due to the injected charges can be envisioned, which is schematically described in Figure 12. When a gate bias of 25 V is applied, a layer of negative charges (purple layer) is formed on the SiO_2 surface around the

CNT (Figure 12 (a)). The CNT channel will experience a net potential from both the gate bias and the injected charges. When the gate bias is decreased, the injected charges cannot dissipate immediately, which means that the potential acting on the CNT channel from the injected charges deceases more slowly than that from the gate potential. When the gate bias decreases to a certain value, the effect from the injected charges will overwhelm that of the polarization induced by the gate bias and turns the transistor on (Figure 12 (b)). This will shift the transfer curve to the right. When V_{gs} = 0 V, the injected charges still exist (Figure 12 (c)) and the transistor remains on. As the gate bias decreases to the negative region, holes are injected onto the SiO_2 surface as shown in Figure 12 (d), compensating the trapped electrons. For a period of time, both holes and electrons will coexist on the SiO_2 surface side by side, as shown in Figure 12. With further decrease of the gate bias, the injected charges will be fully inverted to holes (Figure 12 (e)). This process reverts as the gate bias sweeps back from -25 V to 25 V (Figure 12 (e)-(h)).

One important conclusion that we can draw from this study is that CNT FET cannot be used for memory applications due to two reasons. First, charge dissipation leads to data retention problem. Second, the μm size of the charged area limits data storage density and generates cross talking among cells.

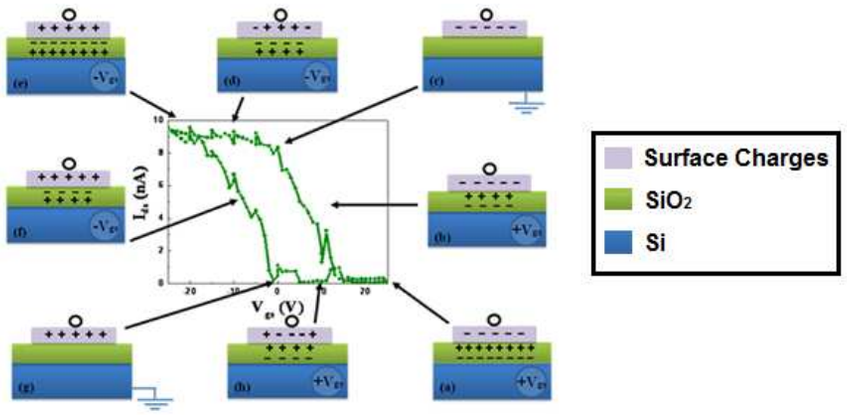

Figure 12. The dynamic screening effect of the injected charges. (a-d) Upon application of a positive gate bias, electrons are injected onto the SiO_2 surface around the CNT channel. When the gate bias is decreased, polarization charge decreases but injected charges remain. Once the gate bias turns negative, holes are injected onto the SiO_2 surface. (e-h) Opposite process takes place when the gate bias is swept from $-V_{max}$ to $+V_{max}$. Reprinted with permission from [40] Copyright 2012, IOP Publishing.

In conclusion, the in-situ EFM study helped us to establish a clear correlation between the charge injection around the CNT and the hysteresis behavior of the transistor. This technique can also be used to study other nanoelectronic devices.

2.3.3. Surface chemistry and hysteresis in CNT FET

We have demonstrated that injected charges around the CNT channel causes the hysteresis in the transfer characteristic of CNT FET. It is natural to ask, what are the charge traps? To answer this question, we have studied the discharging dynamics on SiO_2 surface at different temperatures.

We started with a charging process using the setup shown in Figure 13 (a) where a bias is applied to the electrode as descripted in [44]. When the bias is turned on, we can observe (Figure 13 (b)) that both the EFM phase shift and the width of the charged area increase with charging time. Since a positive tip bias is used during the lift scan, bright contrast in this context represent negative charges, and dark means positive charges.

After the charging process, the electrode is ground and EFM scan is performed on the same area at different time intervals. Figure 13 (c) shows the cross-sectional profile of the recorded EFM data with the CNT at the origin. It is observed that charges next to the CNT diffuse back to the channel immediately after the bias is turned off. This dissipation of charges results in the formation of a peak in the profile which represents the maximum surface charge density. This peak gradually moves away from the CNT as more charges diffuse back to the channel. Using Matlab 7.5, we have fitted the discharging curves at temperatures from 110 °C to 180 °C, and extracted the charge diffusion coefficients at different temperatures.[41] A transition point at 150 °C is observed as shown in Figure 13 (e). Charge dissipation at temperatures below this point experiences a barrier (trap depth) of ~ 0.46 eV, which changes to 0.91 eV at higher temperatures. According to Zhuravlev, SiO_2 surface usually terminates with silonal groups and can absorb water molecules.[42] As temperature increases, these water molecules will be released above a boundary temperature, which ranges from 120 °C to 190 °C depending the structure of silica. (Interested readers are referred to refs [42, 43].) This suggests that the change in the charge diffusion barrier is likely the result of water evaporating from the SiO_2 surface. This is consistent with the claim that water layer acts as the charge traps on SiO_2 surface at room temperature. [33]

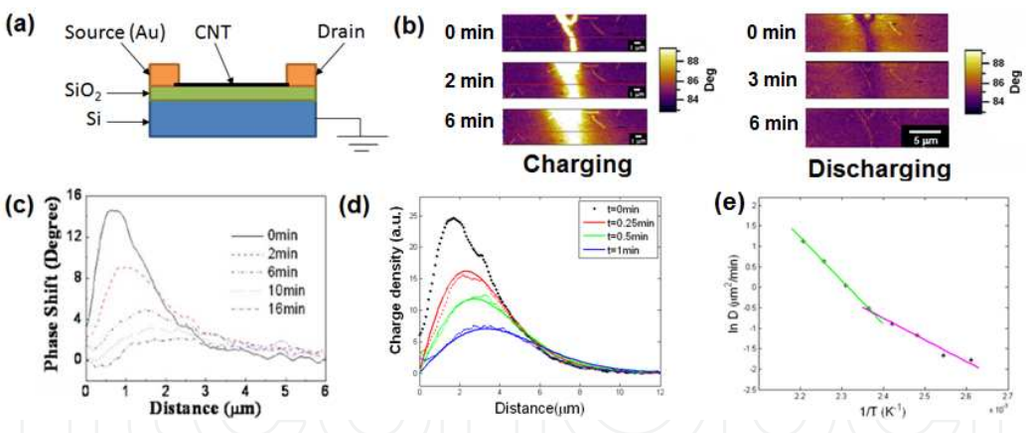

Figure 13. (a) Schematic diagram of experiment setup. (b) Images obtained during the charging and discharging processes. (c) Discharging curves obtained at room temperature. (d) Discharging curves at 180 °C (dotted) and fitting result (line). (e) Temperature dependence of diffusion coefficient reveals the activation energy change at 150 °C. Reprinted with permission from [44], Copyright 2012, American Institute of Physics. Reprinted with permission from [41], Copyright 2012, American Chemical Society.

2.3.4. Eliminating the hysteresis

It is clear that water layer on SiO_2 surface act as charge traps at room temperature. Thus it would be expected that hysteresis in the transfer characteristic can be eliminated simply by increasing the measurement temperature. We conducted transfer measurements at different temperatures ranging from 20 °C to 180 °C and the results are shown in Figure 14 (a, b). As

http://dx.doi.org/10.5772/52067

temperature increases, the hysteresis width continues to decrease, though the scattering of data prevents us from obtaining accurately the activation energy of the evolution and critical temperature if any. It is interesting to note that the hysteresis disappears under negative gate bias at 180 °C and above, but remains under positive gate bias. Figure 14 (c) shows this transition more clearly from 140 °C to 180 °C. At 140 °C, a normal hysteresis (black) loop can still be observed. With an increase of 30 °C in temperature, we can observe that there is a dip (red curve) at around V_{gs} = 5 V. With further increase of temperature, there is a clear shrinkage of the hysteresis loop on the negative bias side. At 180 °C, the loop (green curve) has almost disappeared in the negative V_{gs} region. On the contrary, the loop expanded in the positive V_{gs} region. This clearly indicates that there are two types of charge traps available on the SiO_2 surface. It is likely that evaporation of water at high temperatures results in the SiO_2 surface being dominated by electron trapping defects. If this is true, at 180 °C, where there is little or no hysteresis loop in the negative V_{gs} region, there should not be any injected charges. We conducted EFM imaging at V_{gs} = -10 V at 20 °C and 180 °C as shown in insert of Figure 14 (a). At 20 °C, the dark contrast, indicating positive charges, could be observed and related to the formation of the hysteresis loop (black) in Figure 14 (a). At 180 °C, the absence of dark contrast around the CNT indicates negligible charge injection as compared with that taken at room temperature (inset of Figure 14 (a)). Upon cooling back to room temperature (20 °C), the hysteresis loop can be observed again, as shown in Figure 14 (d). Once the device reaches room temperature (0 min), main part of the hysteresis recovers immediately. However, even after 59 hours under ambient condition, the hysteresis width is still less than the original value. This observation suggests that the first few layers of water is absorbed back onto the SiO_2 surface upon cooling to room temperature, but full recover of the original surface condition takes much longer time.

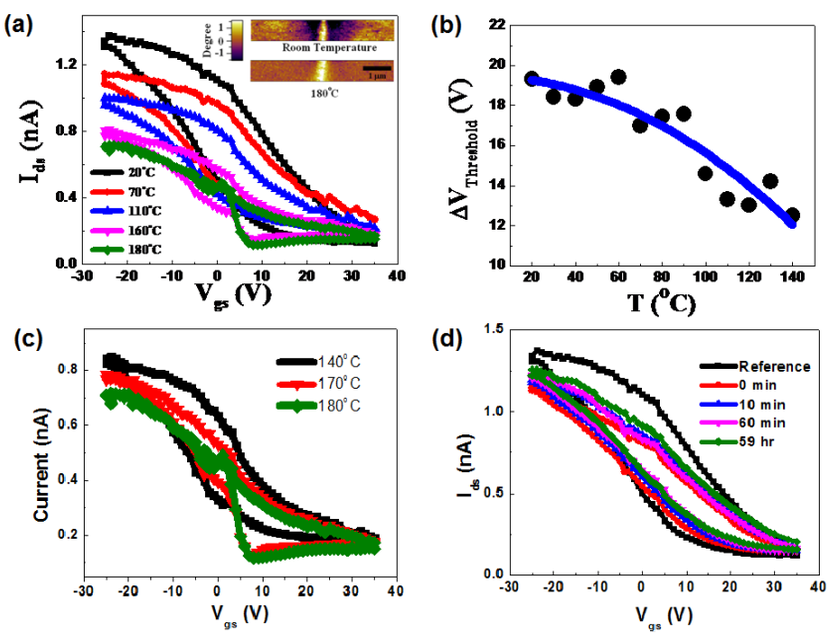

Figure 14. Temperature dependent hysteresis loops. (a) The hysteresis width decreases as temperature increases. At 180 °C, the hysteresis completely disappears under negative gate bias, but remains under positive bias, indicating the lack of hole traps on the SiO_2 surface. (b) The hysteresis width measured by threshold voltage shift at different temperatures. (c) hysteresis loops taken around the transistion temperature depicting the transformation in (a). (d) hysteresis loop time duration study upon cooled down to room temperature. [45]

Our study has demonstrated the effect of SiO_2 surface chemistry on the hysteresis behavior of the CNT FET. It is thus expected that by modifying the SiO_2 surface, we may be able to reduce or even eliminate the charge trapping and thus the hysteresis. In order to confirm this, we have prepared self assembled monolayer (SAM) of Octadecyltrichlorosilane (OTS) as a passivation layer on SiO_2. This was done by dipping the sample with CNTs into the OTS solution for a period of 72 hrs, as it is not possible for CNT to be grown on OTS treated substrates due to the high growth temperature. The sample was then tested by applying a -5 V bias to the CNT through the drain electrode while keeping the gate grounded. Figure 15 shows the results obtained.

The topography of the device has changed as seen in Figure 15 (a). The rougher surface suggests that OTS has formed on the sample surface. Figure 15 (b) shows the EFM charging images around the CNT channel before and after the OTS treatment. It is noted that after OTS treatment, the width of the charged area and the amount of surface charges decreased significantly. Unfortunately, OTS treatment is corrosive in nature and the CNT FET is easily broken after the treatment, preventing us from conducting transfer measurement. Furthermore, the increased surface roughness complicates the study. Other surface treatment techniques should be explored.

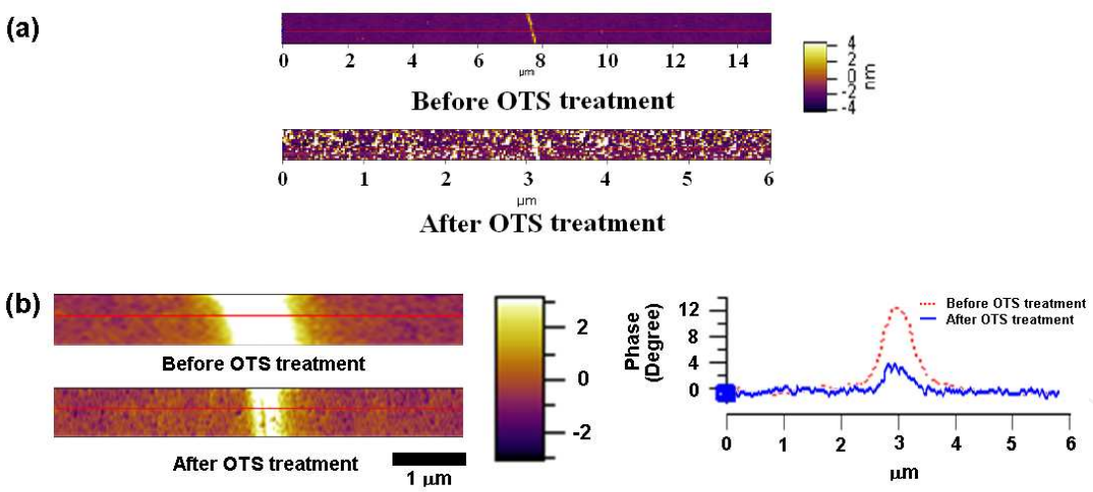

Figure 15. Surface modification with OTS (a) Topography images of sample before and after OTS treatment for 72 hrs. (b) Corresponding EFM images of (a) after charging with -5 V bias. (c) Cross section profiles of EFM images clearly shows the decrease in injected charges.

In summary, we have shown that charge injection around the CNT channel under gate bias causes the hysteresis in the transfer characteristic of the SiO_2-gated CNT FET. We suggest that CNT FET cannot be used for non-volatile memory applications because of data retention and device density issues. As for application in logic devices, surface modification may help to eliminate the hysteresis behavior.

http://dx.doi.org/10.5772/52067

3. Future perpectives

The unique advantages of AFM-based techniques make them ideal for nanoelectronic devices characterizations. Though much has been accomplished, there are still many areas where AFM-based techniques can be of great importance.

One area of interest where AFM-based techniques can be used is the study of sensing devices. In CNT or other nanomaterials-based sensing devices, surface interaction is important for the device functionality. As we have established in the earlier discussion, AFM-based techniques can be used for in-situ imaging with nanometer resolution. It allows users to correlate the charge activites and device performance, which will lead to a better understanding of the device operation mechnaism.

Study on graphene has exploided recently. Most of the works done on CNT that we discussed earlier can be transfered to graphene and graphene based devices. For example, the dynamics performance of graphene-based FET, the tunning of graphene band structure by external fields etc. Furthermore, graphene is structually malleable and its electronic, optical properties are strongly affected by strain. AFM-based techniques can be of great importance in this area of study. Effect of environment and surface chemistry on the properties of graphene can also be investigated using AFM in an variable environment hood. As modern technology continues to evolve into the nano era, AFM-based techniques will certainly become more important in the studies of future nanoelectronic devices.

Acknowledgements

The authors will like to acknowledge the support from Nanyang Technological University, Ministry of Education of Singapore under project number AcRF RG30/06 and National Research Foundation of Singapore under project number NRF-CRP5-2009-04. The authors will also like to thank Dr Li Bing for his help in the OTS sample preparation.

Author details

Hock Guan Ong and Junling Wang*

*Address all correspondence to: jlwang@ntu.edu.sg

School of Materials Science and Engineering
Nanyang Technological University, Singapore

References

[1] Iijima, S. (1991). Helical microtubules of graphitic carbon. *Nature*, 354, 56-58.

[2] Young, R., Ward, J., & Scire, F. (1972). The Topografiner: An Instrument for Measuring Surface Microtopography. *The Review of Scientific Instruments*, 43(7), 999-1011.

[3] Binning, G., Rohrer, H., Gerber, Ch., & Weibel, E. (1981). Tunneling through a controllable vacuum gap. *Applied Physics Letters*, 40, 178-180.

[4] Binning, G., Rohrer, H., Gerber, Ch., & Weibel, E. (1983). 7X7 Reconstruction on Si(111) Resolved in Real space. *Physical Review Letters*, 50(2), 120-123.

[5] Nobelprize.org. (1986). The official Web Site of the Nobel Prize. *The Nobel Prize in Physics Ernst Ruska, Gerd Binnig, Heinrich Rohrer*, http://www.nobelprize.org/nobel_prizes/physics/laureates/1986/, accessed 16 May 2012.

[6] Binning, G., & Quate, C. F. (1986). Atomic Force Microscope. *Physical Review Letters*, 56(6), 930-933.

[7] Mody, C. (2011). Instrumental Community: Probe Microscopy and the Path to Nanotechnology. *MIT Press*.

[8] Sarid, D. (1994). Scanning Force Microscopy. *New York : Oxford University Press*.

[9] Asylum Research Manual v04 _08. (2008). https://support.asylumresearch.com/forum/content.php?4-Software, (accessed Nov.2008).

[10] Kim, J. H., Noh, H., Khim, Z. G., Jeon, K. S., Park, Y. J., Yoo, H., Choi, E., & Om, J. (2008). Electrostatic force microscopy study about the hole trap in thin nitride/oxide/semiconductor structure. *Applied Physics Letters*, 92, 132901.

[11] Lei, C. H., Das, A., Elliott, M., & Macdonald, J. E. (2003). Conductivity of macromolecular networks measured by an electrostatic force microscopy. *Applied Physics Letters*, 83, 482-484.

[12] Mélin, T., Diesinger, H., Deresmes, D., & Stiévenard, D. (2004). Probing Nanoscale Dipole-Dipole Interactions by Electric Force Microscopy. *Physical Review Letters*, 92, 166101.

[13] Lei, C. H., Das, A., Elliott, M., & Macdonald, J. E. (2004). Quantitative electrostatic force microscopy-phase measurements. *Nanotechnology*, 15, 627-634.

[14] Paillet, M., Poncharal, P., & Zahab, A. (2005). Electrostatics of Individual Single-Walled Carbon nanotubes Investigated by Electrostatic Force Microscopy. *Physical Review Letters*, 94, 186801.

[15] Zdrojek, M., Mélin, T., Diesinger, H., Stiévenard, D., Gebicki, W., & Adamowicz, L. (2006). Charging and discharging process of carbon nanotubes probed by electrostatic force microscopy. *Journal of Applied Physics*, 100, 114326.

[16] Domanský, K., Leng, Y., Williams, C. C., Janata, J., & Petelenz, D. (1993). Mapping of mobile charges on insulator surfaces with the electrostatic force microscope. *Applied Physics Letters*.

[17] Jespersen, T. S., & Nygård, J. (2007). Probing induced defects in individual carbon nanotubes using electrostatic force microscopy. *Applied Physics A*, 88, 309-313.

[18] Bactold, A., Fuhrer, M. S., Plyasunov, S., Forero, M., Anderson, E. H., Zettl, A., & Mc Euen, P. L. (2000). Scanned Probe Microscopy of Electronic Transport in Carbon Nanotubes. *Physical Review Letters*, 84, 6082-6085.

[19] Martin, Y., Abraham, D. W., & Wickramasinghe, H. K. (1998). High-resolution capacitance measurement and potentiometry by force microscopy. *Applied Physics Letter*, 52(13), 1103-1105.

[20] Weaver, J. M. R., & Abraham, D. W. (1991). High resolution atomic force microscopy potentiometry. *Journal of Vacuum Science Technology B*, 9(3), 1559-1561.

[21] Schönenberger, C., & Alvarado, S. F. (1990). Observation of Single Charge Carriers by Force Microscopy. *Physical Review Letters*, 65(25), 3162-3164.

[22] Lei, C. H., Das, A., Elliott, M., & Macdonald, J. E. (2003). Conductivity of macromolecular networks measured by an electrostatic force microscopy. *Applied Physics Letters*, 83, 482-484.

[23] Nonnenmacher, M., O'Boyle, M. P., & Wickramasinghe, H. K. (1991). Kelvin Probe Force Microscopy. *Applied Physics Letters*, 58(25), 2921-2923.

[24] Jespersen, T. S. (2007). Nygård Mapping of individual carbon nanotubes in polymer/nanotube composites using electrostatic force microscopy. *Applied Physics Letter*, 90, 183108.

[25] Zhao, M., Gu, Z., Lowther, S. E., Park, C., Jean, Y. C., & Nguyen, T. (2010). Subsurface characterization of carbon nanotubes in polymer composites via quantitative electric force microscopy. *Nanotechnology*, 21, 225702.

[26] Lu, W., Xiong, Y., Hassanien, A., Zhao, W., Zheng, M., & Chen, L. (2009). A Scanning Probe Microscopy Based Assay for Single-Walled Carbon Nanotube Metallicity. *Nano Letters*, 9(4), 1668-1672.

[27] Park, C-J., Kim, Y-H., & Chang, K. J. (1999). Band-gap modification by radial deformation in carbon nanotubes. *Physical Review B*, 60(15), 10656-10659.

[28] Barboza, A. P. M., Gomes, A. P., Archanjo, B. S., Araujo, P. T., Jorio, A., Ferlauto, A. S., Mazzoni, M. S. C., Chacham, H., & Neves, B. R. (2008). A Deformation Induced Semiconductor-Metal Transition in Single Wall Carbon Nanotubes Probed by Electric Force Microscopy. *Physical Review Letters*, 100, 256804.

[29] Shiraishi, M., Takebe, K., Matsuoka, K., Saito, K., Toda, N., & Kataura, H. (2007). Surface potential analyses of single-walled carbon nanotube/metal interfaces. *Journal of Applied Physics*, 101, 014311.

[30] Jespersen, T.S., & Nygård, J. (2005). Charge Trapping in Carbon Nanotube Loops Demostrated by Electrostatic Force Microscopy. *Nano Letters*, 5(9), 1838-1841.

[31] Tans, S. J., Verschueren, A. R. M., & Dekker, C. (1998). Room-temperature transistor based on a single carbon nanotube. *Nature*, 393, 49-52.

[32] Wang, C., Zhang, J., Ryu, K., Badmaev, A., Arco, L. G. D., & Zhou, C. (2009). Wafer-scale fabrication of separated carbon nanotube thin-film transistors for display applications. *Nano Letters*, 9(12), 4285-4291.

[33] Kim, W., Javey, A., Vermesh, O., Wang, Q., Li, Y., & Dai, H. (2003). Hysteresis Caused by Water Molecules in Carbon Nanotube Field-Effect Transistors. *Nano Letters*, 3(2), 193-198.

[34] Radosavljevi, M., Freitag, M., Thadani, K.V, & Johnson, A.T. (2002). Nonvolatile Molecular Memory Elements Based on Ambipolar Nanotube Field Effect Transistors. *Nano Lett.*, 2(7), 761-764.

[35] Fuhrer, M. S., Kim, B. M., Dürkop, T., & Brintlinger, T. (2002). High-Mobility Nanotube TransistorMemory. *Nano Letters*, 2(7), 755-759.

[36] Cui, J. B., Sordan, R., Burghard, M., & Kern, K. (2002). Carbon nanotube memory devices of high charge storage stability. *Applied Physics Letters*, 81, 3260-3262.

[37] Kim, J. H., Noh, H., Khim, Z. G., Jeon, K. S., Park, Y. J., Yoo, H., Choi, E., & Om, J. (2008). Electrostatic force microscopy study about the hole trap in thin nitride/oxide/semiconductor structure. *Applied Physics Letters*, 92, 132901.

[38] Chazalviel, J-N. (1999). Coulomb Screening by Mobile Charges: Applications to Material Science, Chemistry, and Boilogy. *Birkhäuser: Boston*.

[39] Chua, L-L., Zaumseil, J., Chang, J-F., Ou, E. C.-W., Ho, P. K.-H., Sirringhaus, H., & Friend, R. H. (2005). General observation of n-type field effect behavior in organic semiconductors. *Nature*, 434, 194-199.

[40] Ong, H. G., Cheah, J. W., Zou, X., Li, B., Cao, X. H., Tantang, H., Li, L-J., Zhang, H., Han, G. C., & Wang, J. (2011). Origin of hysteresis in the transfer characteristic of carbon nanotube field effect transistor. *Journal of Physics D:Applied Physics*, 44, 285301.

[41] He, Y., Ong, H. G., Zhao, Y., He, S., Li, L-J., & Wang, J. (2009). Study of Charge Diffusion at the Carbon Nanotube-SiO_2 Interface by Electrostatic Force Microscopy. *Journal of Physical Chemistry C*, 113, 15476-15479.

[42] Zhuravlev, L.T. (2000). The surface chemistry of amorphous silica. *Zhuravlev model. Colloids and Surfaces A*, 173, 1-38.

[43] Iler, R. K., editor. (1979). The Chemistry of Silica Solubility, Polymerization, Colloid and Surface Properties, and Biochemistry. New York : Wiley.

[44] Ong, H. G., Cheah, J. W., Chen, L., Tangtang, H., Xu, Y., Li, B., Zhang, H., Li, L-J., & Wang, J. (2008). Charge injection at carbonnanotube-SiO_2 interface. *Applied Physics Letters*, 93, 093509.

[45] Ong, H.G. (2012). Study of Carbon Nanotube Field Effect Transistor Using Electrostatic Force Microscopy. *PhD thesis. Nanyang Technological University.*